Research Square

Preprints are preliminary reports that have not undergone peer review.
They should not be considered conclusive, used to inform clinical practice,
or referenced by the media as validated information.

Synergetic Experimental and ANN- Based Modeling of Cyclic Voltammetry Behavior in NH 4 F-Assisted MnCo 2 O 4 Nanosheet for High-Performance Supercapacitors

Imene Gritli
Research and Technology Center of Energy
Idoumou Bouya Ahmed
The University of Sousse
Zakarya Ahmed
Zalahmed@imamu.edu.sa

Imam Mohammad Ibn Saud Islamic University (IMSIU)
Chemseddine Maatki
Imam Mohammad Ibn Saud Islamic University (IMSIU)
Fehri Krout
Research and Technology Center of Energy
Ibtissem Ben Assaker
Research and Technology Center of Energy

Article

Keywords: MnCo2O4 Nanosheet, stainless steel mesh, effect of NH4F, Artificial neural network based cyclic voltammetry modeling, Supercapacitor Electrodes

Posted Date: March 9th, 2026

DOI: https://doi.org/10.21203/rs.3.rs-8879453/v1

License: This work is licensed under a Creative Commons Attribution 4.0 International License.
Read Full License

Additional Declarations: No competing interests reported.

Synergetic Experimental and ANN- Based Modeling of Cyclic Voltammetry Behavior in NH_4F-Assisted $MnCo_2O_4$ Nanosheet for High-Performance Supercapacitors

Imene Gritli [1], Idoumou Bouya Ahmed [1, 2], Zakarya Ahmed [3*], Chemseddine Maatki[3], Fehri Krout [1], Ibtissem Ben Assaker [1]

* Corresponding Author: Zalahmed@imamu.edu.sa

[1] Nanomaterials and Systems for Renewable Energy Laboratory, Research and Technology Center of Energy, Technoparc Borj Cedria, BP 095, Hammam Lif, Tunisia;
[2] Higher School of Science and Technology of Hammam Sousse, The University of Sousse, Sousse, Tunisia
[3] Department of Chemical Engineering, College of Engineering, Imam Mohammad Ibn Saud Islamic University (IMSIU), 11432, Riyadh, Saudi Arabia

Abstract

$MnCo_2O_4$ nanostructures were chemically deposed on stainless steel flexible substrate with the assistance of NH_4F for their excellent supercapacitor electrodes properties. $MnCO_2O_4$ nanowires and nanosheet were grown on the stainless steel mech through a one-step hydrothermal process using NH_4F. The as prepared nanowires and nanosheet $MnCo_2O_4$ was characterized by XRD, FTIR, SEM-EDX. The XRD spectra of the sample exhibited a face centered cubic phase structure. SEM observations showed that the addition of NH_4F transformed the $MnCo_2O_4$ morphology from nanowires to arrays of nanosheets, anchored onto stainless steel mesh. The electrochemical performance of $MnCo_2O_4$ nanowires and nanosheets was evaluated using EIS, CV and GCD. The associated morphological modification plays a crucial role in enhancing the electrochemical charge storage capability of the supercapacitor electrodes. According to EIS studies, incorporating NH_4F enhances capacitance and charge distribution while reducing charge transfer resistance. The CV and GCD tests confirmed that $MnCo_2O_4$ nanosheet arrays demonstrated improved highest CV-specific capacitance of 318.7 F g^{-1} at 5 mV s^{-1}, aligned with GCD- specific capacitance reaching 769.3 at 1 A g^{-1}. Furthermore, the cyclic voltammetry of the prepared electrodes was successfully predicted using an intelligent artificial neural network (ANN) implemented in Python environment. The proposed ANN model exhibits strong learning capability and high predictive accuracy demonstrating a satisfactory predictive performance with an error below 0.05%. Overall, these results indicate that the developed ANN model, combined with the superior electrochemical performance of the synthesized electrode, holds strong potential for supercapacitor application.

Keywords: $MnCo_2O_4$ Nanosheet, stainless steel mesh, effect of NH_4F, Artificial neural network based cyclic voltammetry modeling, Supercapacitor Electrodes.

1. Introduction

As a result of the growing environmental problems and depletion of fossil fuels, many efforts have been made to investigate renewable energy resources. The development of high-performance electrochemical energy storage systems has been the subject of numerous studies in an effort to meet the growing energy demand an environmental degradation. A promising tool for electrochemical energy storage, supercapacitors have garnered a lot of research interest recently due to their many advantages over batteries and electrostatic capacitors, including high power density, long lifespan, rapidly charge/discharge rates, safe operation, and environmental sustainability[1]. In accordance with the energy storage mechanism of supercapacitors, electrode materials are classified into two major types: electrical double-layer capacitors (EDLCs) and pseudocapacitors[2]. EDLCs storage charges on active materials by electrostatic interaction between ions of the liquid electrolyte and electronic charges on the electrode surface. One common material for electric double layer capacitors is carbon[3]. However, the reversible Faraday redox processes that occur at the electrode-electrolyte interface or close to the surface are the basis for the pseudocapacitors storage mechanism. Furthermore, materials featuring a spinel structure have favorable attributes such a stable chemical profile, varied redox chemistry, high theoretical capacitance, and a green profile. During electrochemical analysis, the spinel structure' greater specific surface area and favorable ionic transport characteristics increase the current density and promote faster ionic movement. To date, several spinel structures, including $NiCo_2O4$[4], $CuCo_2O4$[5], $MnCo_2O4$[6], $ZnCo_2O4$[7], $ZnFe_2O4$[8], $NiMn_2O4$[9] and $CoMn_2O4$[10], have been synthesized and shown to exhibit supercapacitor properties. Several chemical techniques, such as sol-gel, co-precipitation, microwave, hydrothermal and electrodeposition synthesis, have been employed to prepare metal-based spinel oxides. Among them, manganese-cobalt oxides $MnCo_2O_4$ have garnered a lot of interes because of their availability, low cost, non toxicity and attractive application as supercapacitor electrodes[1] and[6] and[10] and[11] and[12]. $MnCo_2O_4$ crystallizes in a normal spinel structure, where Mn^{2+} ions occupy the tetrahydral sites, Co^{3+} reside in the octahedral sites, and O^{2-} anions coordinate both cationic positions, resulting in a face-centered cubic lattice[13]. and As with many spinel-type materiels, the relatively low electronic conductivity of $MnCo_2O_4$ remains a major limitation for its practical implementation in energy storage applications. To address this issue, numerous strategies have been reportred, including nanostructures engeneering, composite formation, cation doping, carbon-based surface modification, and the creation of porous or hollow architectures to enhace the specific surface area. Futhemore, due to their low cost, accessibility, and environmental friendliness, soluble inorganic salts like NH_4F have been used more effectively than nanostructuring and coating with differents type of carbon in tailoring the morphology of metal oxides acting as templating or surfactant agents, and in decreasing the crystallinity of fluorine-rich structures[14]. Chen, et al. hypothesize that F^- can active the substrate to create active sites for nucleation[15]. Zeng et al. identify two main functions of F^-, combine with the cations and anions to form intermediates and, the ionic hydration effect of fluorine F-. Water molecules can be bounded and structured around the F^-, which has an indirect impact and rise the average activity coefficients of ions in solutions[16]. While NH_4F's exact role in influencing morphological changes is not completely understood[17]. Some researchers have recently reported composite $MnCo_2O_4$ morphologies prepared using various techniques techniques including NH_4F-assisted methods. S. Al-Rubaye et al prepared a nanoflakes $MnCo_2O_4$ throught the hydrothermal method in combininations with the graphene nanoplates deposited on Ni foam using an electrophoretic deposition technique demonstrated a specific capacitance of 1268 Fg^{-1} at 1 mVs^{-1}. Additionnaly a study has shown that the addition of NH_4F during hydrothermal procees resulting in the further nucleation and growth of new surface on top of the flakes morphology[18]. Owing to its low cost, good electrical conductivity, environmental friendliness, and excellent mechanical strength combined with corosion resistance, stainless steel mesh has emerged as a promising substrate

for supercapacitor electrode application. Its three- dimentionnal porous architectures facilitates efficient electron transport and electrolyte penetration. Morever the hydrothermal growth of $MnCo_2O_4$ directly on enexpensive SS mech offers considerable potentiel for further improving electrode performance in supercapacitor systems. Based in the above, we suggest that the $MnCo_2O_4$ distictives nanostructures are crucial to its capacity to store charge. The performance of $MnCo_2O_4$ can be effectively enhaced by a simple hydothermal approach on flexible SS mech with NH_4F-assisted morphology control.

On the other hand, various approaches have been proposed to evaluate the performance of supercapacitpors. Conventional mathematical and electrical models generally provide accurate performance descreption. However, they are often complex and computationnaly demanding[19]. In recent years, artificial intelligence techniques, particularly artificial neural networks (ANN) have emerged as powerful alternatives due to their fast computation, ease of implementation, and strong learning copabilities. Inspired by biological neural systems, ANN can model both linear and nonlinear behaviors without requiring explicit physical models or governing aquations, as input and output relationships are learned from experimental data. In this context, our research group has previously demonstrated the effectiveness of ANN modeling by successfully comparing experimental and theoretical electrochemical results in an earlier combined metal oxyde materials study on mixed metal oxide materials deposited on a stainless steel substrate[20]. These charcteristics make ANNs especially suitable for estimating complex and nonlineair systems. Navertheless, several studies have demonstrated the potential of ANN based approaches for supercapacitors analysis, such as modeling thermal and electrical behaviors and predicting energy conversion and management performance, highlighting the relevance of ANN methods for advanced supercapacitor modeling[21, 22].

In This work we reprted the synthesis of $MnCo_2O_4$ through a one-step hydrothermal process coated stainless steel mech. For the first time we investigated the synergitic experimental and artificial neural network- based cyclic voltammetry behavior model of as prepared $MnCo_2O_4$ elctrodes. At the outset, the effect of the NH_4F additive on the structural, morphological, and electrochemical properties of the prepared electrodes is examined. Subsequently, the cyclic voltammetry behavior of the electrodes is modeled using an intelligent artificial neural network (ANN) implemented in a Python environment. Finally, the correlation between experimental and theoretical results is analyzed and discussed.

2. Materials and Methods

2.1. Preparation of $MnCo_2O_4$ with different morphologies on stainless-steel mesh (SSM)

All chemicals were of analytical reagent grade, bought from Sigma Aldrich, and utilized exactly as supplied requiring no additional purification. the substrate was cleaned using Hydrochloric acid (37 %), 2- propanol (99.8 %), and acetone (99.5 %). In order to prepare $MnCO_2O_4$ as a supercapacitor electrode, a rectangular piece of stainless-steel mesh with a wire diameter of 35 µm and a screening dimension of 45 µm was divided into a square form measuring 1 cm by 3 cm. The cobalt chloride [$CoCl_2 \cdot 6H_2O$], Manganese chloride tetrahydrate [$MnCl_2.4H_2O$], urea [$CO(NH_2)_2$], ammonium fluoride [NH_4F] were used to deposit $MnCo_2O_4$ onto a stainless-steel mesh via the hydrothermal method.

As mentioned in the introduction part, several techniques have been used to obtain metal-based spinel oxides[1, 3, 4, 23]. In the present study, $MnCo_2O_4$ was prepared through a hydrothermal method followed by calcination with varying ratios of ammonium fluoride. Initially, SSM was cut into a rectangular piece (1× 3 cm) and cleaned by immersion in hydrochloric acid, then was sequentially cleaned with acetone and isopropanol for 10 minutes each

followed by distilled water rinsing. To prepare the precursor solution, 1 mmol manganese chloride tetrahydrate ($MnCl_2.4H_2O$), 2 mmol cobalt chloride ($CoCl_2.6H_2O$), 5 mmol urea $[CO(NH_2)]_2$ and varying amounts of NH_4F (0, 5, 10, 15, or 20 mmol) were dissolved in 40 ml of deionized water and stirred thoroughly for 10 minutes. The resulting homogeneous solution was transferred into a 50 mL Teflon-lined stainless-steel autoclave. The SSM pieces were immersed vertically at a 45° angle against the inner wall of the autoclave. The hydrothermal reaction was conducted at (120 °C) for 6 hours. Following naturally cooling to ambient degree, coated mesh was taken off and repeatedly washed about distilled water in order to rid of any remaining solvent. Finally, the prepared SSM was calcinated at 400 °C for three hours.

The synthesized $MnCo_2O_4$-coated SSM samples were used as electrodes for supercapacitors and labeled as MCO 0, MCO-5, MCO-10, MCO-15, and MCO-20. The number denotes the molar amount (mmol) of NH_4F used, while MCO represents $MnCo_2O_4$. Fig. 1 illustrates a schematic representation of the synthesis process.

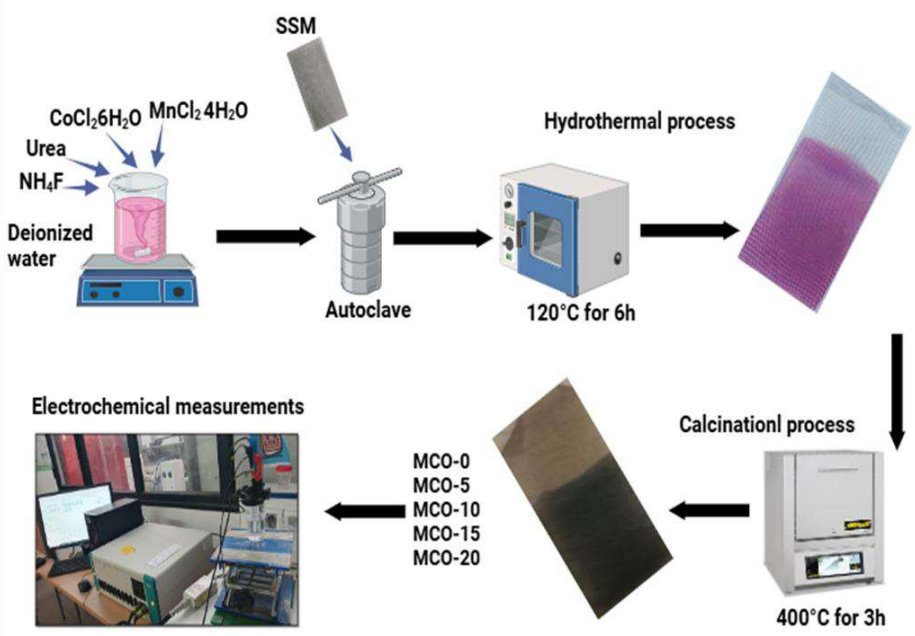


Fig. 1. Flowchart depicting the experimental procedure for synthesizing $MnCo_2O_4$ (MCO) on stainless steel mesh (SSM).

2.2. Characterization

The crystalline phase and structural purity of the prepared MCO electrode were analyzed using X-ray diffraction (XRD) using a Bruker D8 Advance diffractometer (Bragg–Brentano geometry) equipped with Cu Kα radiation (λ = 1.54 Å) and operated at 40 kV and 40 m. The 2θ range of 20° to 70° was used to record the diffraction patterns. Fourier transform infrared spectroscopy (FTIR) was performed using a Bruker spectrometer in the range of 400–4000 cm^{-1} to analyze the functional groups of $MnCo_2O_4$. A Hitachi S-4800 scanning electron microscope (SEM) was used to analyze the catalysts' surface morphology. Using energy-dispersive X-ray spectroscopy (EDX), the elemental composition was ascertained. All electrochemical analysis of $MnCo_2O_4$ electrode were carried out using an Autolab potentiostat/galvanostat. Electrochemical impedance spectroscopy (EIS), cyclic voltammetry (CV) and galvanostatic charge-discharge (GCD) tests were used to investigate the supercapacitive properties of

$MnCo_2O_4$ electrodes. All tests were conducted in an inert 1M KOH electrolytic solution at ambiant temperature. EIS was carried out with an applied voltage to the signal of 10 mV throughout a frequency range of 100 KHz to 0.01 Hz. After fitting the EIS data, the analogous circuit was modeled using ZView® 4.0 computer program. Equation (1) was used to calculate the specific capacitance (Cs) from the cyclic voltammetry curves.

$$C_s = \frac{\int_{Va}^{Vc} IdV}{m\nu(V_c - V_a)} \quad (1)$$

The instantaneous current, I, the mass of the active electrode material excluding the SSM substrate, m (g), and the voltage scan rate, ν (mV s^{-1}) are used to calculate the specific capacitance over the potential window defined by V_c and V_a, representing the upper and lower voltage limits of the voltammetric curve (V), respectively. Furthermore, the specific capacitance (C_s) was evaluated from the galvanostatic charge-discharge measurements according to Equation (2).

$$C_s = \frac{I\Delta t}{m\Delta V} \quad (2)$$

2.3. Artificial neural network- based cyclic voltammetry behavior model

This study investigates the application of an artificial neural network (ANN) for predicting current–potential curves in electrochemical systems at different scan rates of MCO-15 electrode. ANN model for testing cyclic voltammetry behavior at different scan rates was implemented and executed in a Python environment. Experimental data collected at scan rates of 5, 10, 30, 50, 70, and 100 mV/s were cleaned and normalized prior to model development. A feedforward ANN model was implemented and trained using the Levenberg–Marquardt with pyrenn optimization algorithm. A schematic diagram for an artificial neuron network architecture for CV behavior modeling is shown in Fig. 2. The diagram illustrates a 2-10-1 artificial neural network (ANN) developed to model the nonlinear relationship between potential, time, and current. The input layer consists of two neurons (potential and time) connected to a hidden layer of ten neurons through synaptic weights and biases, followed by a non-linear activation function. The output layer contains a single neuron that receives the hidden layer outputs via weights and provides the estimated current. The network is a fully connected feedforward architecture, trained by adjusting the weights and biases to minimize the error between predicted and experimental current values.

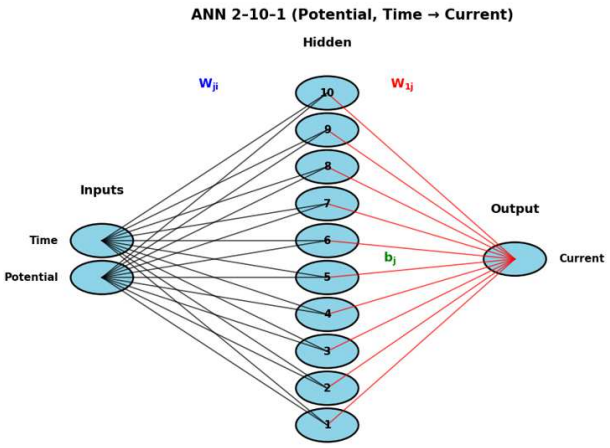


Fig. 2. Artificial neural network architecture.

Details of the ANN model's training parameters and architecture are provided in Table1.

Table 1. Artificial neural network parameters and architecture.

ANN paramaters	Vlue/Type
Number of neuron at imput	2
Number of neuron at output	1
Number of neuron at hidden layer	10
Objective of function	Mean Absolute Error (MAE)
	Root Mean Square Error (RMSE)
The initial weights and biases	Random
Activation function	Sigmoid activation function
Learning rule	Levenberg–Marquardt with pyrenn propagation algorithm

The prediction error corresponds to the difference between the experimental currents density (I_{exp}), and the ANN predicted current density (I_{ANN}), as given in Equation

$$e\,(k) = I_{exp}(k) - I_{ANN}(k) \quad (3)$$

where K representes the sumple number

ANN performance during trining was assesed using the mean absolute error (MAE) and the root mean squared error (RMSE) as expressed in equation (4) and (5) respectively.

$$MAE = \frac{1}{N}\sum_{i=1}^{N}|e(k)| \quad (4)$$

$$RMSE = \sqrt{\frac{1}{N}\sum_{i=1}^{N} e^2(k)} \quad (5)$$

Where N refers to the number of data samples.

3. Results and discussion

3.1. Structural study

Fig. 3 (a) displays the X-ray diffraction (XRD) patterns of $MnCo_2O_4$ samples before the addition of NH_4F (MCO-0) and after its addition (MCO-5, MCO-10, MCO-15, MCO-20). Regardless of the NH_4F concentration, all spectra exhibit diffraction peaks at 43.12° and 50.36°, which originate from the stainless-steel mesh substrate. All other peaks were identified as characteristic of $MnCo_2O_4$, as confirmed by JCPDS card no. 23-1237[24]. The characteristic diffraction peaks at 2θ values of 30.89°, 36.39°, 38.5°, 44.2°, 55.35°, 58.76°, and 64.61° are cubic spinel $MnCo_2O_4$, respectively[25]. No diffraction peaks corresponding to second phase like Co_3O_4 and MnO_2 were detected, demonstrating the high purity of the $MnCo_2O_4$ products that were obtained[18]. Xiaoqiang et al.[26] formed hydrothermally $MnCo_2O_4$ nanowires and nanosheet arrays on nickel foam and validated this behavior and found

that corresponding diffraction are assigned to JCPDS card no, 23-1237 of $MnCo_2O_4$. Similarly, Zhu et al.[27] synthesis a pure phase of $MnCO_2O_4$ using hydrothermal method on nickel foam substrate.

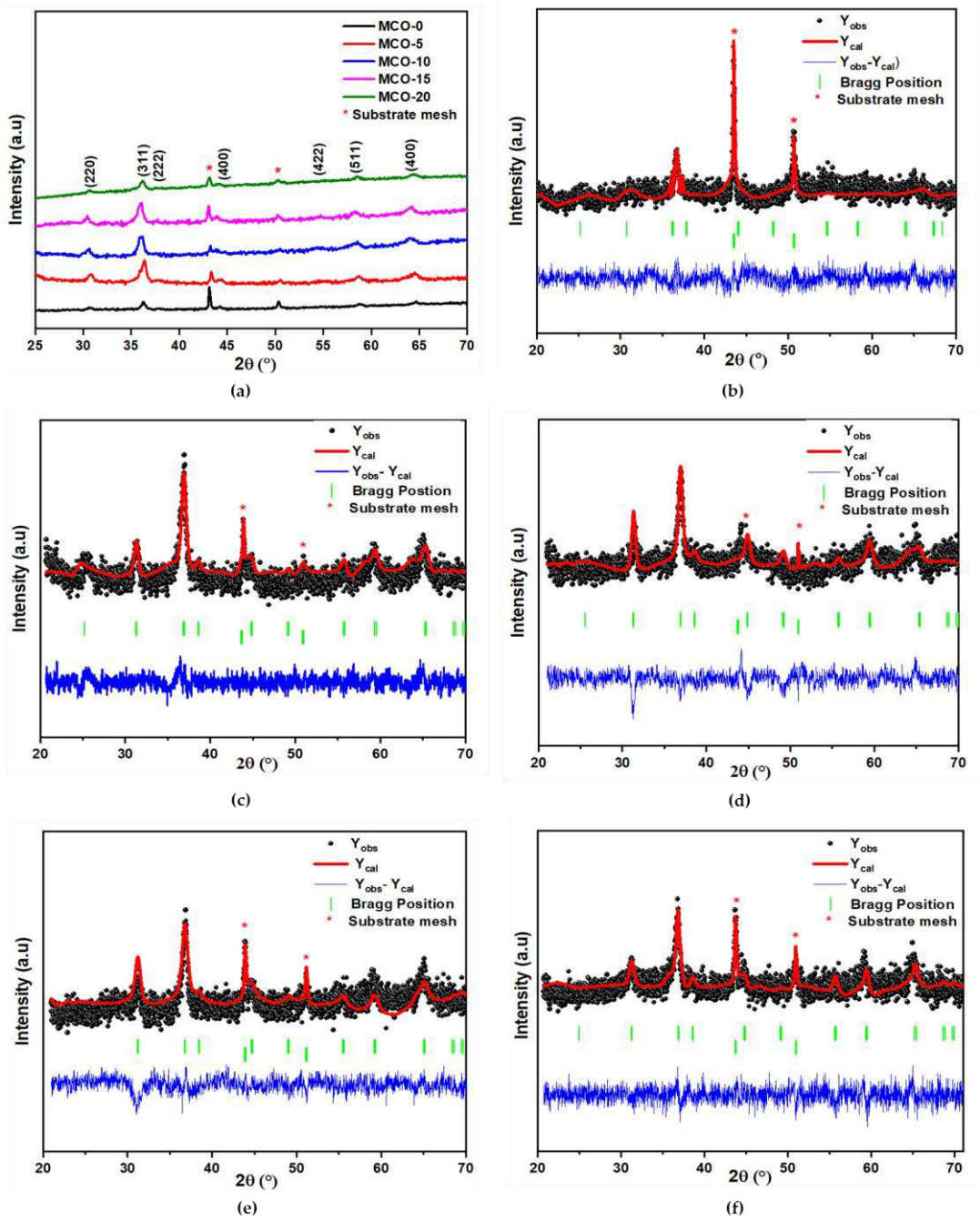


Fig. 3 (**a**) Superposition of XRD Spectra, and ; (**b**) MCO-0, **(c)** MCO-5; **(d)** MCO-10 **;(e)** MCO-15; **(f)** MCO-20 experimental XRD Data and Rietveld Models.

The effect of the amount of NH_4F on crystalline parameters: crystallite size and dislocation density were studied. So, the average crystallite size of the $MnCo_2O_4$ film was estimated using the Debye-Scherrer formula (Equation (6)) by analyzing the most intense diffraction peak (311) of $MnCo_2O_4$.

$$D = \frac{K\lambda}{\beta\cos\theta} \quad (6)$$

Here, D denotes the crystallite size, K is the shape factor of the crystallites (0.9), λ represents the X-ray wavelength (0.154 nm), β is the full width at half maximum (FWHM), and θ is the diffraction angle. The dislocation density (δ) of the samples was determined using the equation proposed by Williamson and Smallman (Equation (7)).

$$\delta = \frac{1}{D^2} \quad (7)$$

Table 2 provides a summary of the computed values for each physical parameter for the samples. The data indicates that the presence of NH_4F may reduce the crystallinity of $MnCo_2O_4$ during the growth process. A comparable pattern was noted by Waghmode et al[28], who observed a decrease in crystallite size during the hydrothermal synthesis of $NiCo_2O_4$. Using the FullProf Suite program, the Rietveld refinement was carried out to further confirm the purity of the obtained samples with different NH_4F ratios. The Rietveld method is applied using the FullProf program to refine the space group and lattice parameters through profile matching with a constant scale factor, as shown in Figures 2b–f. The refinement results shown again the existence of two separate phases, one is for $MnCo_2O_4$ spinel and another is for stainless steel mesh substrate. The precise cell parameters and some of the important Rietveld analysis values (lattice parameter a), including Rp (profile R-factor), Rwp (weighted profile R-factor) and χ2 (goodness-of-fit parameter) are shown in Table 2.

Table 2. Rietveld refinement parameter and XRD data summary of MCO samples.

Samples	(a=b=c) (Å)	Rp (%)	Rwp (%)	X^2	D (nm)	(δ) $\times 10^{14}$ (m^{-2})
MCO-0	8.22	11.6	5.5	1.5	53.16	3.5
MCO-5	8.08	9.9	5.4	1.2	35.45	7.9
MCO-10	8.07	12.6	6.6	1.4	15.18	43.4
MCO-15	8.10	10.4	6.4	1.3	35.42	8.1
MCO-20	8.08	11.7	6.3	1.2	21.26	22.1

3.2. Spectroscopy FTIR Analysis

FTIR analysis was used to identify the stretching and bending vibrations of spinel tetrahedral and octahedral complexes present in the samples. The FTIR spectrum of $MnCo_2O_4$ was recorded in the range of 400–4000 cm^{-1}, as shown in Fig. 4.

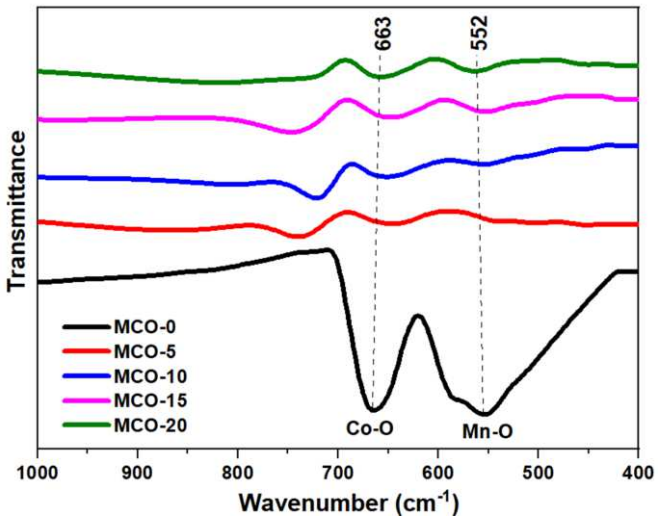


Fig. 4 FTIR spectra overlay of $MnCo_2O_4$ samples.

Two absorption bands were observed at 663 cm^{-1} and 552 cm^{-1}, corresponding to cobalt-oxygen (Co–O) bonding vibrations in tetrahedral sites and manganese-oxygen (Mn–O) bending vibrations in octahedral sites, respectively. In accordance with earlier publications[29] regarding $MnCo_2O_4$, these two bands can be attributed to the Mn^{+} and Co^{3+} oxygen bond stretching vibration, respectively. Fig. 4 also shows that $MnCo_2O_4$ (MCO-0) devoid of NH_4F displays the characteristic absorption bands of cobalt and manganese at 553 cm^{-1} and 661 cm^{-1}, respectively. With the addition of NH_4F in different amounts (MCO-5, MCO-10, MCO-15, and MCO-20) throughout the hydrothermal process, the strength of these absorption bands progressively diminishes. This pattern is in line with the XRD finding, demonstrating that the $MnCo_2O_4$ structure's crystallinity decreases at the NH_4F percentage rises. These findings further validate that the synthesized material is a crystalline $MnCo_2O_4$ phase, as corroborated by the XRD analysis in Fig. 3.

3.3. Morphological Analysis

The microstructures of $MnCo_2O_4$ samples synthesized with varying NH_4F concentrations (0–20 mmol) were investigated using a scanning electron microscope, as Fig. 5 illustrates. The morphology of MCO-0 without NH_4F at magnetization levels of 200 µm and 20 µm is shown in Fig. 5 (a) and (b). In the absence of NH_4F as a complexing

agent, the final product displayed initial material growth that partially covered the wire of the SSM substrate. Notably, Fig. 5 (b) clearly reveals that the morphology consists of interwoven and interconnected needle-like structures[30]. After adding NH_4F to the hydrothermal solution, a complete coverage of the mesh threads is clearly observed in Fig. 5 (c). The SEM images as shown in Fig. 5 (d) reveal the formation of needle-like nanowires that uniformly cover the entire surface of the stainless-steel mesh. These nanowires continue to extend in length, exhibiting varying degrees of interlacing[7,31]. As shown in Fig. 5 (e) and (f), increasing the NH_4F concentration to 10 mmol led to the emergence of nanosheet structures, resulting in a morphological transformation from needle-like nanowires to a nanosheet@nanowire heterostructure[30]. Fig. 5 (f) clearly illustrates the appearance of clustered needle-like nanowires at the edges of hexagonal nanosheets, which are largely covered by the nanowires. This mixed structure is believed to enhance electrochemical performance. Theoretically, this transformation can be attributed to the lower fluoride ion concentration at reduced NH_4F levels, leading to a slower coordination rate between F^- anions and metal cations. Further increasing the NH_4F concentration to 15 mmol caused significant morphological changes in the $MnCo_2O_4$ nanostructure, as shown in Fig. 5 (g–h). The nanowire structures completely disappeared, and nanosheet structure remained in charge[30]. Magnified SEM images (Fig. 5 (g–h) reveal that many nanosheets assembled into bundles, with most exhibiting a rectangular shape[31]. The presence of 15 mmol NH_4F promotes nucleation and the formation of new nanosheets on existing surfaces, creating an inter-linking network. As NH_4F concentration increases, the number of nuclei (n) also rises, accelerating nanosheet nucleation and improving the structural adhesion between nanoarchitectures and the stainless-steel mesh. In figures 5 (i–j), the MCO-20 structure on the stainless-steel mesh exhibits a nanosheet-like morphology, similar to that observed in Fig. 5 (g) and 5 (h). However, with an increased NH_4F concentration of 20 mmol, the nanosheets become thicker and some aggregates were observed. This structural evolution further demonstrates how strongly the metal oxide material adheres to the substrate.

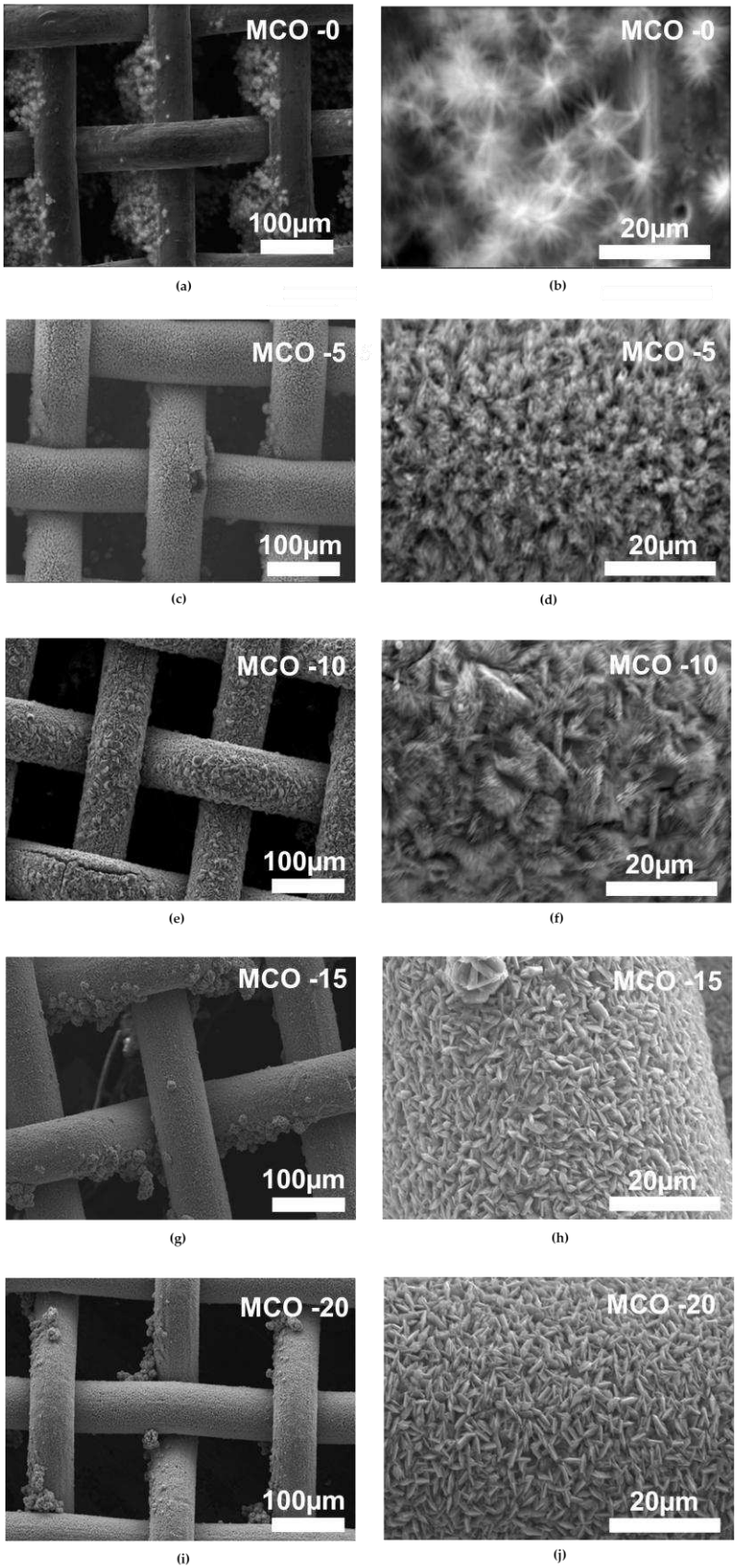


Fig. 5. SEM micrographs of $MnCo_2O_4$ with different amount of NH_4F: **(a–b)** 0 mmol; **(c–d)** 5 mmol; **(e-f)** 10 mmol; **(g–h)** 15 mmol; **(i-j)** 20 mmol.

3.4. Mechanism illustration of the different $MnCo_2O_4$ morphologies

Equation (8) can be used to express the chemical reaction of NH_4F that took place during the hydrothermal method:

$$NH_4^+ + F^- + H_2O \leftrightarrow NH_3 \cdot H_2O + HF \quad (8)$$

The urea molecule may be decomposed initially to produce CO_2 and NH_3 ion the precursor solution, and then a hydrolysis reaction proceeds to produce hydroxide ions OH^- equation (9 and 10).

$$NH_2CONH_2 + H_2O \leftrightarrow 2NH_3 + CO_2 \quad (9)$$

$$NH_3 + H_2O \rightarrow NH_4^+ + OH^- \quad (10)$$

The hydroxyl ion product combines with Mn and Co ions to form manganese -cobalt hydroxide film which can then be deposed on the SS surface by Vander Waals forces (equation (11)).

$$Mn^{2+} + 2Co^{2+} + 6OH^- \rightarrow MnCo_2(OH)_6 \quad (11)$$

Manganese-cobalt oxide film was produced as a result of the decomposition of manganese-cobalt hydroxide film during post-annealing in the air equation (12).

$$MnCo_2(OH)_6 + {}^1/_2\ O_2 \rightarrow MnCo_2O_4 + 3H_2O \quad (12)$$

Inorganic salts like NH_4F have proven effective in modifying the morphologies of metal oxides, serving as surfactants or template agents. They are environmentally friendly, cost-effective, and readily available, making them preferable to organic additives. Additionally, NH_4F serves as a morphology-controlling agent to explore the electrochemical properties of $MnCo_2O_4$ nanostructures that are dependent on their morphology[32]. The proposed growth mechanism of $MnCo_2O_4$ nanosheets and nanowires synthesized with various NH_4F concentrations is illustrated in Fig. 6, demonstrating their potential for high-performance hybrid supercapacitors.

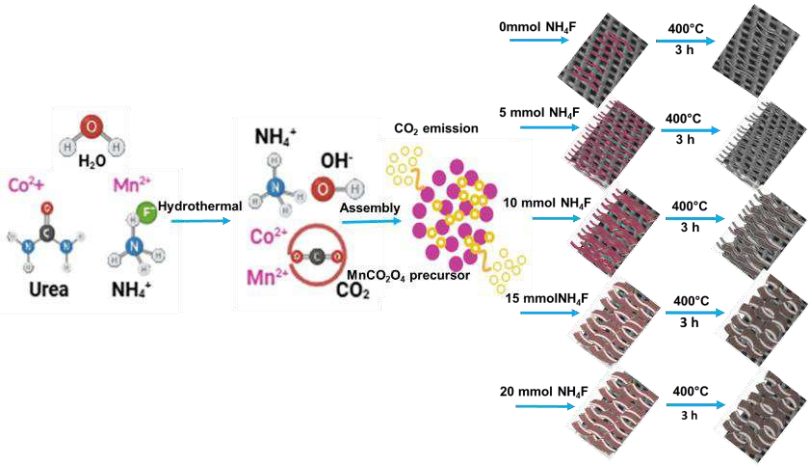


Fig. 6. Growth mechanism of $MnCo_2O_4$ with varying morphologies influenced by NH_4F.

These hard anions (F^- ions) easily attack and adsorb to $MnCo_2O_4$, thus the higher the concentration (like fluoride ions) of anions in solution, it has been proven that the rate of F^- Anions are also faster high coordination between metal cations and ion in solution. This faster formation rate for n cycle can cause swift evolution of nanosheet to different stages (nucleation, growth) that eventually formed with higher specific surface area. With the increase in the reactant (NH_4F) concentration, speed of nucleation process can be accelerated by increasing the nucleic number(n), but nanosheet grow up maybe slowly. F^- anions can be employed to activate the MCO substrate, thereby promoting growth and nucleation by providing a higher concentration of active sites. This activation would enhance the strong adhesion of the hierarchies with the MCO and promote its electrochemical performance.

3.5. Energy Dispersive X-ray (EDX) spectroscopy

To determine the chemical composition of the synthesized samples, energy dispersive X-ray (EDX) spectroscopy was employed to analyze the surface characteristics. As depicted in Fig. 7 (a), the obtained MCO-15 films primarily consist of cobalt (Co), manganese (Mn), and oxygen (O), with additional peaks corresponding to iron (Fe), chromium (Cr), and silicon (Si), which are attributed to the SSM[33]. Atomic compositions and weight percentage of the elements in nanowire architectures are demonstrated in Fig. 7 (b). The Mn: Co atomic ratio of the as-prepared MCO-15 material was 1:2, in good accordance with the theoretic value of 2, verifying the achieved stoichiometry default material of the mixed oxide $MnCo_2O_4$. Furthermore, Fig. 7 (c) shows elemental mapping images that illustrate how manganese, cobalt and oxygen are evenly spread out across the $MnCo_2O_4$ structure. These elemental mapping results, along with X-ray diffraction (XRD) and Fourier-transform infrared (FTIR) analyses, further validate the successful growth of $MnCo_2O_4$ on the stainless-steel mesh without any other metal oxides.

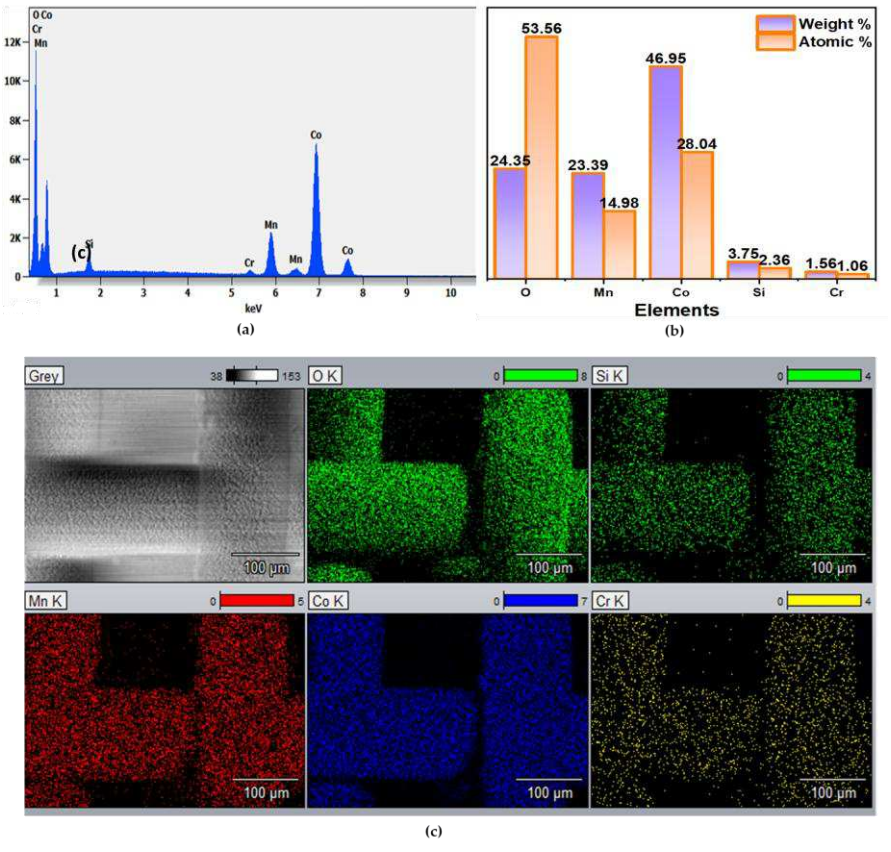


Fig. 7. (a) EDX; **(b)** quantitative analysis; **(c)** elemental mapping of $MnCo_2O_4$ sample.

3.6. Electrochemical measurements

3.6.1 Electrochemical impedance spectroscopy (EIS)

Electrochemical impedance spectroscopy (EIS) was used to examine the charge-transfer characteristics at the electrode/electrolyte interface throughout a frequency range of 100 KHz to 0.01 Hz. A semicircular feature at high frequencies, representing the charge transfer resistance (Rct), and a linear zone at low frequencies, representing the Warburg impedance (Ws) resulting from semi-infinite diffusion, are characteristic features of the ensuing Nyquist plot[34-36]. The $MnCo_2O_4$ (MCO-0) electrode, which was manufactured without NH_4F, has a noticeable semicircle, which corresponds to a high Rct value of 100 ohms, as seen in Fig. 8 (a). When NH_4F is added, the semicircle's diameter is much decreased, Indicating improved charge transfer kenetics[37]. The charge transfer resistances for the NH_4F modified samples (MCO-5, MCO-10, MCO-15, and MCO-20) were deduced from equivalent circuit to be 58, 59, 15, 10, and 14 ohms, respectively.

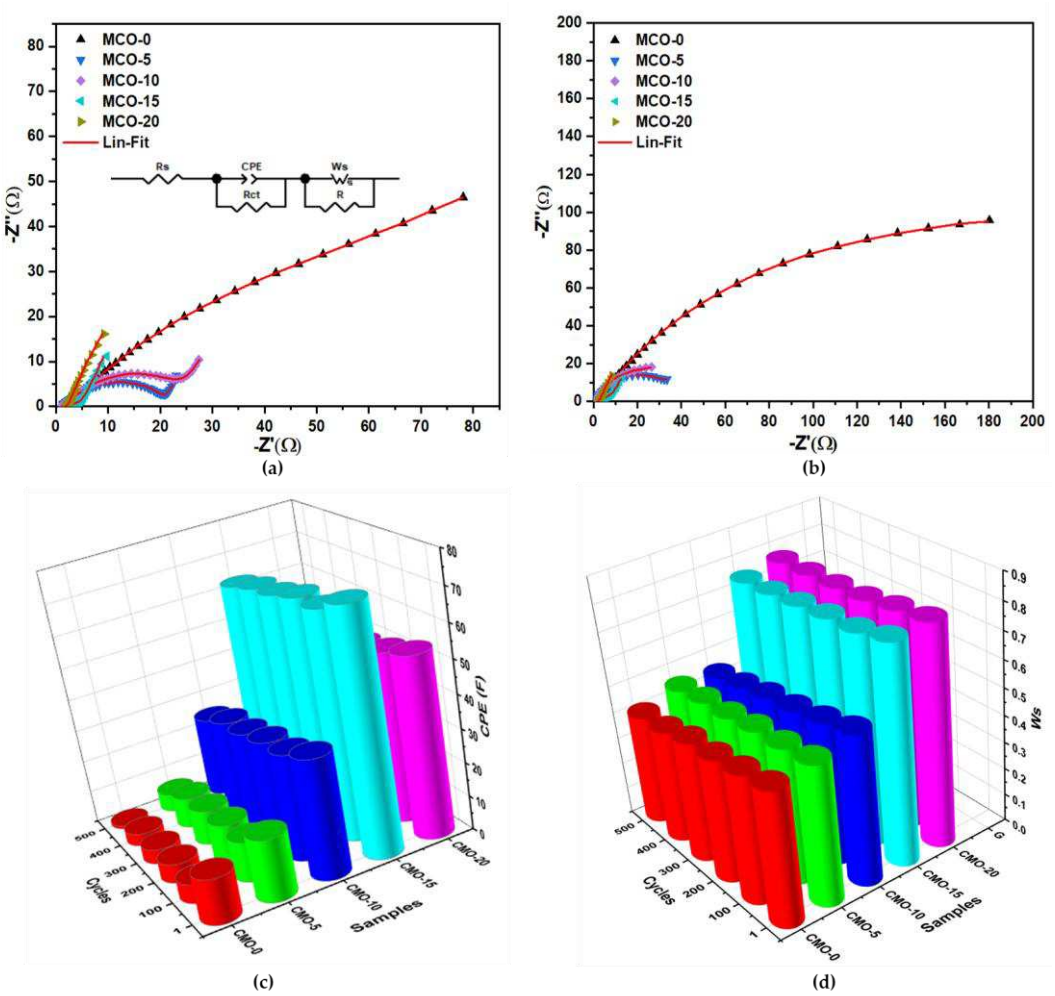


Fig. 8. (a) Impedance spectra of samples prior to cycling; **(b)** Impedance spectra after 500 cycles; **(c)** Variation of the constant phase element (CPE) as a function of cycle number (0, 100, 200, 300, 400, and 500 cycles) for each sample; **(d)** Warburg impedance coefficient (Ws) versus cycle number for each sample.

Interestingly, the lower Rct value reflects faster electron/ion transport across the electrode/electrolyte interface contributing to improved electrochemical performance. The improved Warburg impedance diffusion characteristics and increased specific capacitance (Fig. 8(b) demonstrate the better electrochemical performance, which is correlated with the observed decrease in Rct. The morphological changes brought about by NH_4F, which encourage effective ion diffusion end ease charge storage, are responsible for these improvements. NH_4F changes the $MnCo_2O_4$ surface into a nanosheet shape, increasing the electroactive surface area and lowering electron transport barriers, according to scanning electron microscopy (SEM) study. Furthermore, the long-term cycling stability tests (Fig. 8 (c) and (d) reveal that MCO-15 and MCO-20 exhibit consistent electrochemical performance over 500 cycles, whereas MCO-10 experiences show a noticeable reduction in both capacitance and ion transport efficiency. The use of NH_4F has demonstrated similar effects in other transition metal oxides. For example, A. A. Radhi and colleagues observed that introducing NH_4F during the synthesis of $FeCo_2O_4$ led to a marked reduction in charge transfer resistance, enabling smoother electron and ion mobility across the electrode- electrolyte interface[32]. Similarly, R. Waghmode et all. demonstrated that changes in the morphology of $NiCo_2O_4$ electrodes, brought about by the presence of NH_4F, significantly influenced their electrochemical behavior[28]. Taken together, these findings and the results of the present study highlight the effectiveness of using NH_4F to fine-tune material morphology, offering a promising route to improve the performance of charge storage systems.

3.6.2. Cyclic voltammetry CV

The cyclic voltammetry (CV) properties of the $MnCo_2O_4$ electrodes (MCO-0, MCO-5, MCO-10, MCO-15, and MCO-20) were studies with a three-electrode setup, as shown in Fig. 9 (a). Electrochemical characterization was performed using a 1 M KOH aqueous electrolyte, scanning from –0.4 to 0.5 V (vs. Ag/AgCl) at a sweep rate of 5 mV. Compared to electrodes prepared without NH_4F, the CV profiles exhibit a well-defined pseudo-rectangular shape, indicative of pseudo-capacitive behavior[35]. It is interesting that the CV curve shape does not change much with different NH_4F concentrations, indicating the impressive rate performance of $MnCo_2O_4$ nanowires and nanosheets. It can be determined from that the redox reaction at 5 mV s^{-1} was originated from the oxidation and reduction of $MnCo_2O_4$ in an alkaline electrolyte[38]. The introduction of OH^- ions to the nanostructures implies good electrolyte wettability and it is indicated that NH_4F can facilitate the growth of specific surface area. The potential redox reaction equations of $MnCo_2O_4$ in a KOH electrolyte are presented in Equation (13)-(15)[39, 40].

$$MnCo_2O_4 + H_2O + OH^- \leftrightarrow 2CoOOH + MnOOH + e^- \quad (13)$$

$$MnOOH + OH^- + \leftrightarrow MnO_2 + H_2O + e^- \quad (14)$$

$$CoOOH + OH^- \leftrightarrow CoO_2 + H_2O + e^- \quad (15)$$

Fig. 9 (b) summarizes the specific capacitance value determined using Equation (1) for all electrode at a measurement rate of 5 mVs^{-1}. The results highlight the beneficial effect of adding NH_4F, which enhances the distribution area of the $MnCo_2O_4$ electrode, thereby improving electrical conductivity and ionic mobility at the electrode/electrolyte interface. However, beyond an NH_4F concentration of 15 M, the specific capacitance declines markedly, in agreement with electrochemical impedance spectroscopy (EIS) results, which indicate reduced ion diffusion. These findings corroborate previous studies, affirming that NH_4F is essential for enhancing the performance of

charge storage. In fact, T. Liu et al. proved that the mixed morphology of nanosheet and nanowires which is accomplished by adding 7 mmol of NH_4F, is largely responsible for the exceptional electrochemical properties of CO_3O_4 [7].

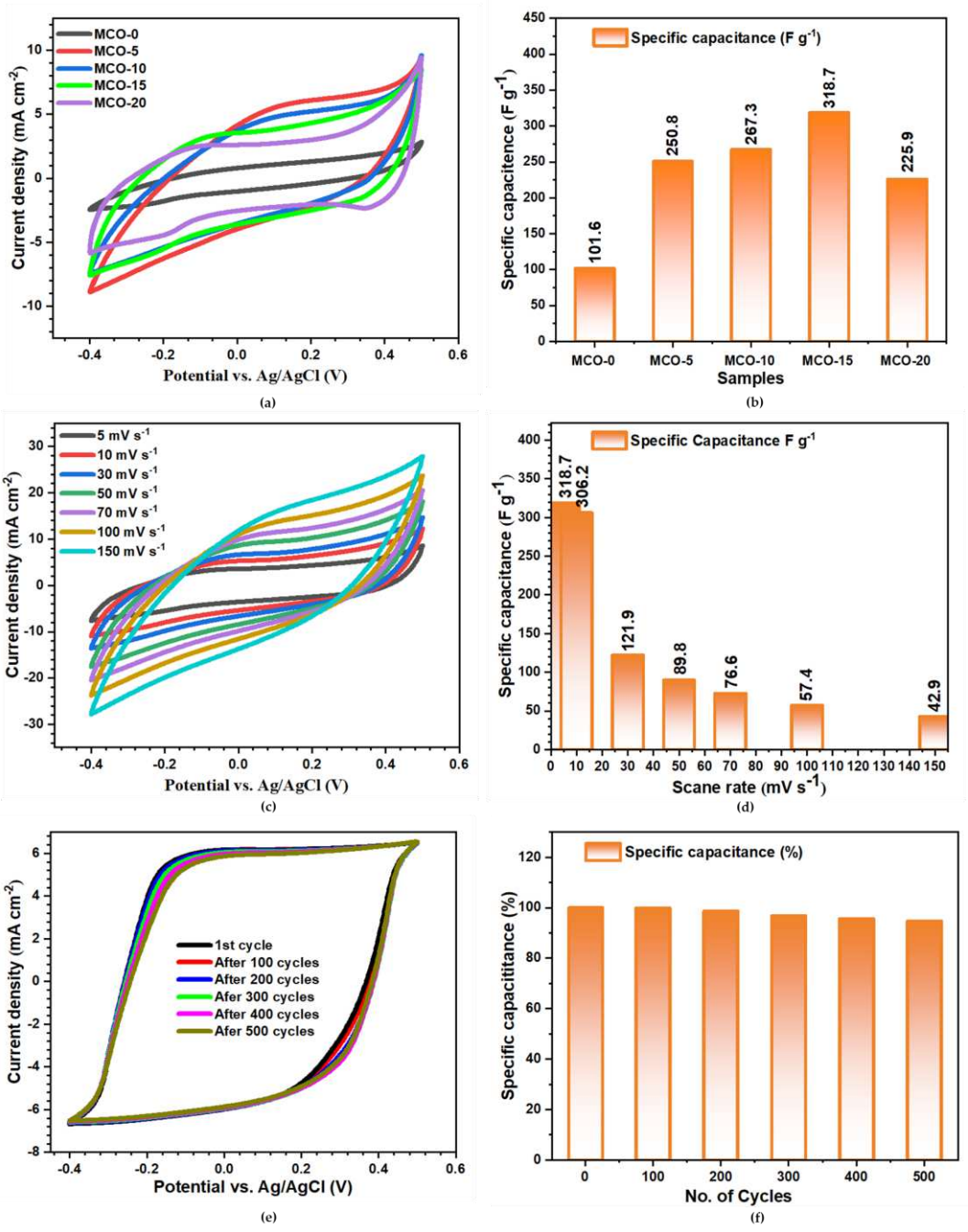


Fig. 9. (a) Cyclic voltammograms (CVs) of the samples recorded at a scan rate of 5mV s^{-1}; **(b)** Specific capacitance of the electrodes calculated from CV at 5 mVs^{-1}; **(c, d)** CV curves and corresponding specific capacitance values of MCO-15 at different scan rates; **(e, f)** CV curves and associated specific capacitance of MCO-15 at different cycle numbers, recorded at a scanning rate of 50 mV s^{-1}.

As illustrated in Fig. 9 (c), an increase in scan rate results in a systematic expansion of the area under the cyclic voltammetry curve of the prepared electrodes, while the overall shape of the curve remained largely unchanged. This behavior indicates good electrochemical reversibility of the electrodes. Furthermore, Fig. 9 (d) displays the capacitance measurements of MCO-15 at various scan rates. The specific capacitance exhibited a noticeable decline from 318 to 42.9 Fg^{-1} as the scan rate increased from 5 to 150 mVs^{-1}, indicating the influence of ion diffusion limitations at higher scan rates. This decline is attributed to the reduced intercalation time at higher scan rates, which limits electrolyte ion penetration to only surface-active sites at the electrode-electrolyte interface, thereby reducing the accessibility of the bulk active material[41]. Long-term cycling experiments were conducted to evaluate the electrochemical stability of the MCO-15 electrode; the results are displayed in Fig. 9 (e). The cyclic voltammetry curves for the 1st to 500th successive cycle show retention of electrochemical performance over the cycling of this long-term experiment. Overall, EIS analysis also supports high capacitance retention and ionic diffusion stability even after 500 complete cycles, as shown in Figures 7c and 7d. Fig. 9 (f) illustrates the percentage of capacitance retention over 500 cycles, indicating the MCO-15 electrodes demonstrated very high cycling stability and robustness. This excellent cycling performance may be ascribed to the structural stability of the interconnected nanosheet like morphology of the materials. This inter-linking network morphology could be desirable to disperse the strass that are created during the prolonged intercalation/deintercalation mechanism of anions.

To further understand the charge storage behaviors, Capacitive and diffusion- controlled contributions are the two primary influencing elements. The diffusion effect is connected to the battery type response procedure whereas the capacitive effect results from the adsorption and desorption of ions on the surface of the electrode. According to Dunn's approach the overall current in CV curves is represented by the sum of capacitive and diffusive responses. To elucidate the influence of NH_4F on the energy storage mechanism, the relationship between the current response (i) and the scan rate (υ) was investigated as described by the following equation (16):

$$i = a\upsilon^{b} \tag{16}$$

The value of constants a and b are especially important. A b-value near 1.0 typically points to a capacitive, surface-driven process, while a value closer to 0.5 is characteristic of diffusion-limited insertion[42]. For most nanostructured anode materials, the b-value generally falls between 0.5 and 1.0, indicating that both capacitive and diffusion - based processes participate in the total amount of charge storage[43]. Fig. 10 presents the linear fitting curves of log(i) versus log(ν) of MCO-0, MCO-5, MCO-10, MCO-15 and MCO-20 used to determine the b-values of the cathodes. The MCO-15 and MCO 20 electrodes cathodic peaks were determined to have b-value of 0.09 and 0.86, subsequently. These values demonstrated a primarily capacitance- controlled behavior, as they were substantially higher than those of MCO-0, MCO-5, and MCO-10 (0.52, 0.72, and 0.73, respectively (Fig. 9 (a-e))[44].

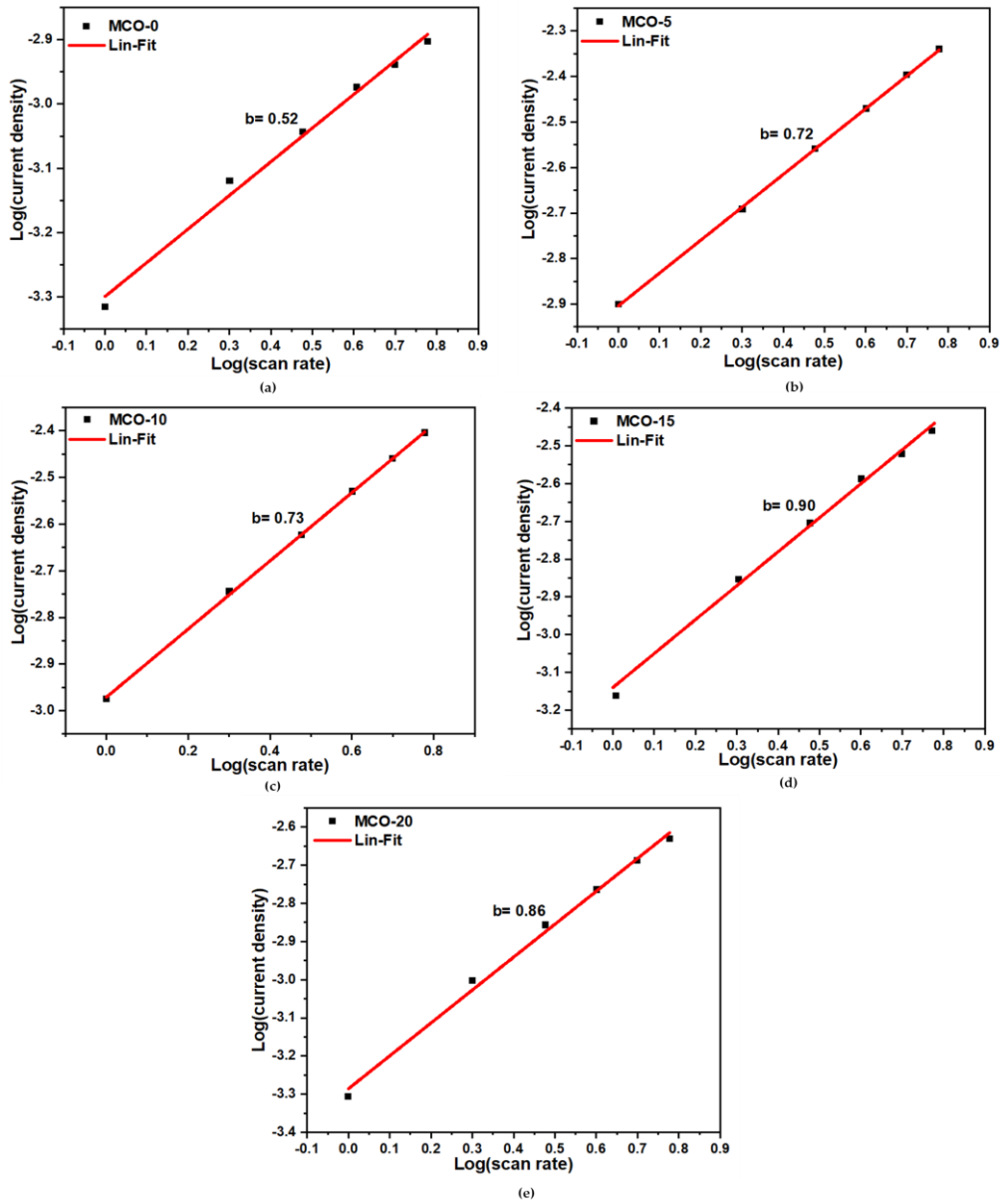


Fig. 10. Plots illustrating the relationship between peak current and scan rate for samples with **(a)** MCO-0; **(b)** MCO-5; **(c)** MCO-10; **(d)** MCO-15; and **(e)** MCO-20 cycles.

Additionally, the contribution ratio of diffusion- controlled and capacitive process were measured using Equation (17)[45].

$$i = k_1\upsilon + k_2\upsilon^{1/2} \quad (17)$$

In this formula, i(v) represents the current response at a specific voltage, comprising two components: $k_1\upsilon$ (capacitive contribution) and $k_2\upsilon^{1/2}$ (diffusion-controlled contribution). Fig. 11 presents the relative contributions of surface capacitive and diffusion- controlled process for the MCO-0, MCO-5, MCO-10, MCO-15 and MCO-20 electrode. It's found that the improved charge storage performance of the MCO-15 electrode mainly comes from the domination of the surface capacitive mechanism (Fig.11 (d)).

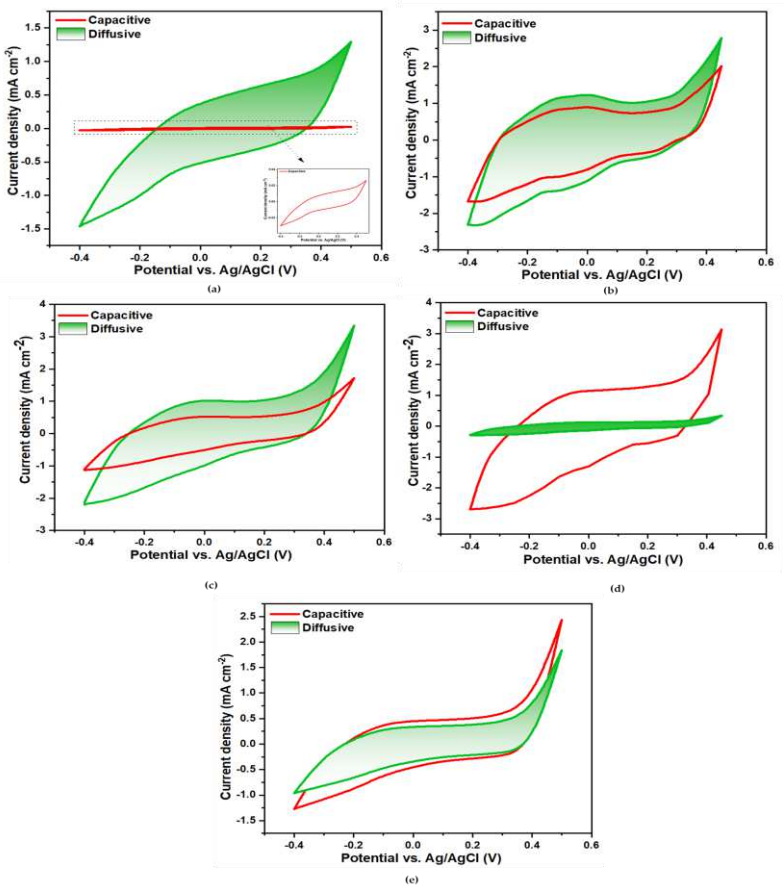


Fig. 11. Simulated CV curves illustrating the separation of capacitive and diffusive contributions for samples with **(a)** MCO-0; **(b)** MCO-5; **(c)** MCO-10; **(d)** MCO-15; and **(e)** MCO-20.

As shown in Fig. 12 (a–e), the capacitive contribution ratio for the MCO-15 electrode was 90.3%, significantly higher than those of MCO-0, MCO-5, MCO-15, and MCO-20, which were 3.8%, 33.4%, 34.3%, and 57.2%, respectively. A thorough analysis of these contribution may be seen in Fig. 12 (a–e). Especially, this highlights the superior fast charging–discharging characteristics of the MCO-15 electrode. Additionally, the capacitive contribution increased with the scan rate[46], ranging from 1 to 6 mV s^{-1}. The MCO-15 electrode demonstrated enhanced OH^- ion diffusion within the electrode material, enabling ultra-fast OH^- ion storage.

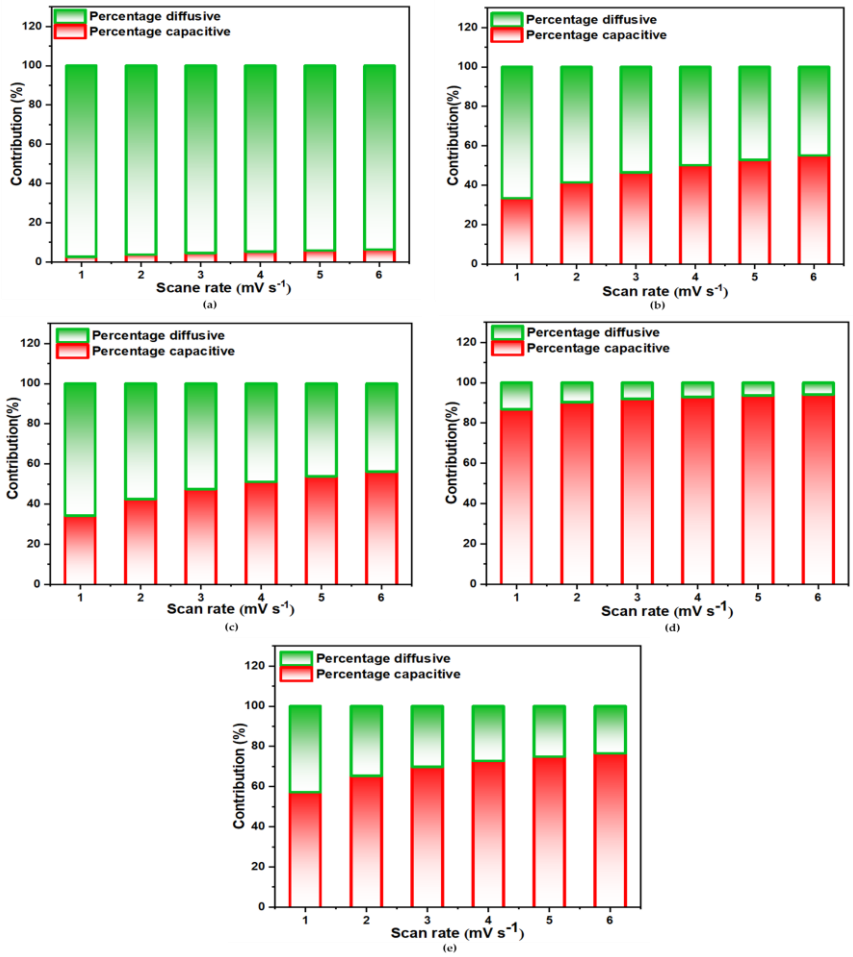


Fig. 12. Analysis of capacitive and diffusive contributions at different scan rates for samples with **(a)** MCO-0; **(b)** MCO-5, **(c)** MCO-10; **(d)** MCO-15; and **(e)** MCO-20 cycles.

3.6.3. Galvanostatic Charge-Discharge (GCD)

Accordingly, Fig. 13 shows the specific capacitances of the MCO electrode that was measured at a constant current's density of 1 mA.cm^{-2}. The computed value at the current density of 1mA.cm^{-2}. The computed value at the current density is 42.5, 632.2, 424.5, 769.3 and 271,6 Fg^{-1} for MCO-0, MCO-5, MCO-10, MCO- 15, and MCO-20, respectively, as shown in Fig. 13 (b).

These values agree with the cyclic voltammetry (CV) results, further supporting the electrochemical trends observed. The deviation from an ideal triangular CV profile indicates the dominance of faradaic charge storage mechanisms, consistent with a pseudocapacitive behavior[47]. Comparing the tested electrodes together, MCO-15 exhibited the highest specific capacitance (769.3 F g^{-1}), aligning with the findings from CV and EIS analyses, highlighting its superior charge storage capability.

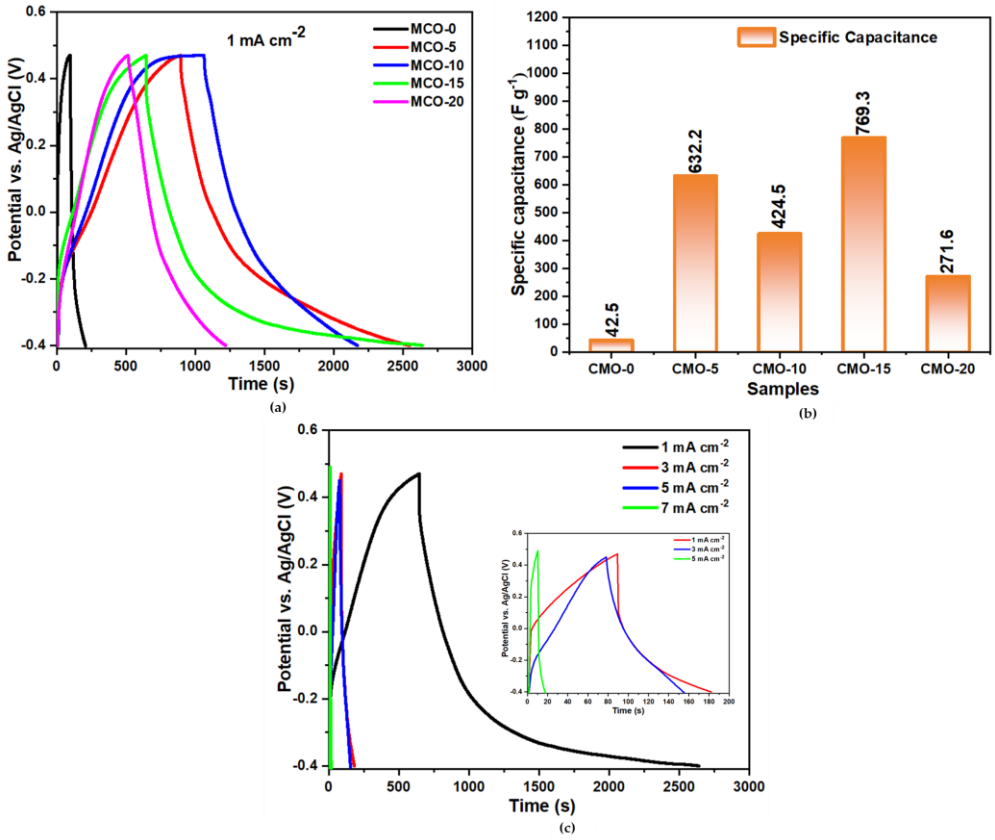


Fig. 13. (a) GCD curves of $MnCo_2O_4$ (MCO) at current density 1 mA cm^{-2}; **(b)**Specific capacitance of electrode determined using GCD at 1 mA cm^{-2}; **(c)** Galvanostatic Charge Discharge curves of MCO-15 at various current range.

The improved electrochemical properties of the $MnCo_2O_4$ nanosheet, such as specific capacitance and conductivity, are due to the tow different cations present in the bimetallic $MnCo_2O_4$ structure[48] and the particular form of nanosheet[49]. The charge storage mechanism of $MnCo_2O_4$ is governed by the redox transitions of Co(III)/Co(II), Co(IV)/Co(III), and Mn(III)/Mn(II), as described by Equations (13)–(15)[40]. The comparative data summarized in Table 3 clearly illustrates that the both morphology and substrate selection significantly influence the electrochemical performance of $MnCo_2O_4$ based electrodes. As an example, Xu et al.[50] mentioned a high specific capacitance of 845.6 F g^{-1} using porous nanorod arrays grown on Ni foam, whereas Che et al.[51] obtained 249.3 F g^{-1} for flower-like hollow microspheres. Gopi et al.[52] fabricated flower-like ZnO@$MnCo_2O_4$ nanosheets on Ni foam, yielding 452.5 F g^{-1}, while Anjana et al.[53] demonstrated that self-organized $MnCo_2O_4$ nanoneedles grown on Ni foam could deliver 420 F g^{-1}. Kuang et al.[54] synthesized mesoporous $MnCo_2O_{4.5}$ nanoneedle arrays on Ni foam, yielding 517.9 F g^{-1}, and Maile et al.[55] employed potentiostatic electrodeposition to obtain binder-free nanoflakes on stainless steel, achieving 585 F g^{-1} at 0.2 mA cm^{-2}. Zhu et al.[56] further improved performance by in-situ growing hollow spheres on Ni foam, reaching 648.4 F g^{-1}.

Table 3. Summary of capacitive characteristics of $MnCo_2O_4$ spinel-based electrodes with varying morphologies for supercapacitors.

Electrode	Morphology	Solution	Substrate	Synthesis Method	Cs (F g^{-1})	Source
$MnCo_2O_4$	nanorods	2 M KOH	Ni foam	Coprecipitation	845.6 (1 A g^{-1})	[50]
$MnCo_2O_4$	ollow microspheres	2 M KOH	Ni sheet	Hydrothermal	249.3 (0.5 A g^{-1})	[51]
ZnO@$MnCo_2O_4$	hierarchical flower	3 M KOH	Ni foam	Hydrothermal	452.5 (1 A g^{-1})	[52]
$MnCo_2O_4$	nanoneedles	1 M KOH	Ni foam	Hydrothermal	420 (5 mV s^{-1})	[53]
$MnCo_2O_{4.5}$	nanoneedle	3 M KOH	Ni foam	Hydrothermal	517.9 (3.6 A g^{-1})	[54]
$CoMn_2O_4$	nanoflakes	1 M KOH	SS	Potentiostatic	585 (0.2 mA m^{-2})	[55]
$CoMn_2O_4$	hollow spheres	1 M Na_2SO_4	Ni foam	Solvothermal	648.4 (2 mV s^{-1})	[56]
$CoMn_2O_4$	nanosheets	1 M KOH	SSM	Hydrothermal	769.3 (1 A g^{-1})	This work

Cs: Specific Capacitance

SSM: Stainless Steel Mesh

In comparison, in this work $MnCo_2O_4$ nanosheets immediately grown on stainless steel mesh provide a specific capacitance of 769.3 F g^{-1} at 1 A g^{-1}. This value not only exceeds most previously reported morphologies, especially those on stainless steel, but also comes lose to the best results obtained with Ni foam. Stainless-steel mesh is an appealing choice due to its low cost, strong mechanical stability, and large surface area, providing a practical and scalable substitute for Ni foam. The outstanding performance observed here is attributable to the nanosheet architecture, which raises the electroactive surface and promotes efficient electron and ion transport. Overall, these results emphasize how careful structural design, together with the selection of affordable substrates, can significantly improve charge-storage performance and move $MnCo_2O_4$ electrodes closer to real-world applications.

3.6.4. Comparison between experimental and theoretical results

An intelligent modeling approach was selected as an appropriate framework to capture the nonlinear oxidation–reduction dynamics observed in voltametric current–potential responses. The intelligent model of ANN was trained using the Levenberg–Marquardt (LM) algorithm, a nonlinear optimization technique that minimizes the squared error between predicted outputs and experimental data. Prior to training, the input and output variables were normalized using Min–Max scaling, and the dataset was partitioned into training (70%), validation (15%), and testing (15%) subsets to ensure robust model evaluation. The performance of the ANN was assessed using the mean absolute error (MAE), the root mean squared error (RMSE) across all subsets and the regression coefficient R^2 which reflects the correlation between the predicted outputs and the target values. The MSE, RMSE and R^2 results of the ANN model for different scan during the training, validation and training phases are presented in Table 4.

Table 4. ANN model performance results.

Scan (mV s^{-1})	Training			Validation			Testing		
	MAE	**RMSE**	**R^2**	**MAE**	**RMSE**	**R^2**	**MAE**	**RMSE**	**R^2**
5	$1.93e^{-5}$	$2.88e^{-5}$	0.999	$2.21e^{-5}$	$3.18e^{-5}$	0.999	$2.13e^{-5}$	$2.86e^{-5}$	0.999
10	$2.73e^{-5}$	$3.61e^{-5}$	0.999	$2.89e^{-5}$	$3.56e^{-5}$	0.999	$2.49e^{-5}$	$3.19e^{-5}$	0.999
30	$5.04e^{-5}$	$6.05e^{-5}$	0.999	$5.93e^{-5}$	$6.91e^{-5}$	0.999	$4.24e^{-5}$	$5.99e^{-5}$	0.999
50	$3.97e^{-5}$	$5.04e^{-5}$	0.999	$3.96e^{-5}$	$4.84e^{-5}$	0.999	$5.05e^{-5}$	$5.05e^{-5}$	0.999
70	$3.89e^{-5}$	$4.71e^{-5}$	0.999	$4.07e^{-5}$	$4.86e^{-5}$	0.999	$4.13e^{-5}$	$4.75e^{-5}$	0.999
100	$4.73e^{-5}$	$6.23e^{-5}$	0.999	$4.62e^{-5}$	$6.38e^{-5}$	0.999	$4.7e^{-5}$	$5.95e^{-5}$	0.999
150	$3.58e^{-5}$	$4.58e^{-5}$	0.999	$4e^{-5}$	$4.96e^{-5}$	0.999	$3.48e^{-5}$	$4.33e^{-5}$	0.999

The results in Table 4 indicate that Levenberg-Marquart algorithm is effective for ANN training validation and testing. The strong agreement between experimental and predicted values is evidenced by MAE, RMSE values close to zero and consistently high (R^2) value (R^2>0.999) across the training, validation and testing stages, with an overall regression of 0.999, confirming the reliability of the proposed model. An artificial neural network (ANN) was implemented as an intelligent modeling tool to predict the cyclic voltammetry behavior of the $MnCo_2O_4$ supercapacitor electrode. Fig.14 compares the ANN predictions with the experimental CV results at scan rates of 5, 10, 30, 50, 70, 100 and150 mV s^{-1}.

Table 5. comparative analysis of experimental results and ANN model predictions

Scan rate (mV s^{-1})	Specific Capacitance by CV (Fg^{-1})	Specific Capacitance by ANN (Fg^{-1})	Error (in %)
5	318.69	318.66	0.01
10	306.16	306.10	0.02
30	121.98	121.92	0.05
50	89.76	89.75	0.01
70	76.63	76.60	0.04
100	57.35	57.19	0.27
150	42.85	42.57	0.65

A strong agreement is observed between the experimental data and the curves generated by the model, demonstrating the ability of the ANN to accurately reproduce the electrochemical behavior of the electrode. Based on the predicted data, the calculated specific capacitance value was 318.66, 306.10, 121.92, 89.75,76.60, 57.19, 42.57 Fg^{-1} corresponding to scan rates of 5, 10, 30, 50, 70, 100, 150 mV s^{-1}. As presented in Table 5, the percentage error defined as the between experimental supercapacitor results and ANN predicted value is found to be very low indicating the satisfactory performance of the proposed ANN algorithm in modeling the cyclic voltammetry curves MCO-15 electrode. These results demonstrate that the artificial neural network (ANN) model is well suited for predicting non-linear behavior, as evidenced by the close agreement with experimental data, particularly in supercapacitor energy storage applications. In this framework, Alimi et al. employed an Artificial Neural network (ANN) model implemented in MATLAB to model and simulate an MnO_2/NiO/ZnO trijunction for supercapacitor application [20]. In addition, W.Z. Tawfik et al developed tow- Layer ANN model based on Machine learning (ML) to provide accurate regression- based prediction of the specific capacitance of porous carbon-based supercapacitors [57]. The significance of theoretical models in predicting performance and optimizing supercapacitor application was also highlighted by G.J Adekoya et al [58].

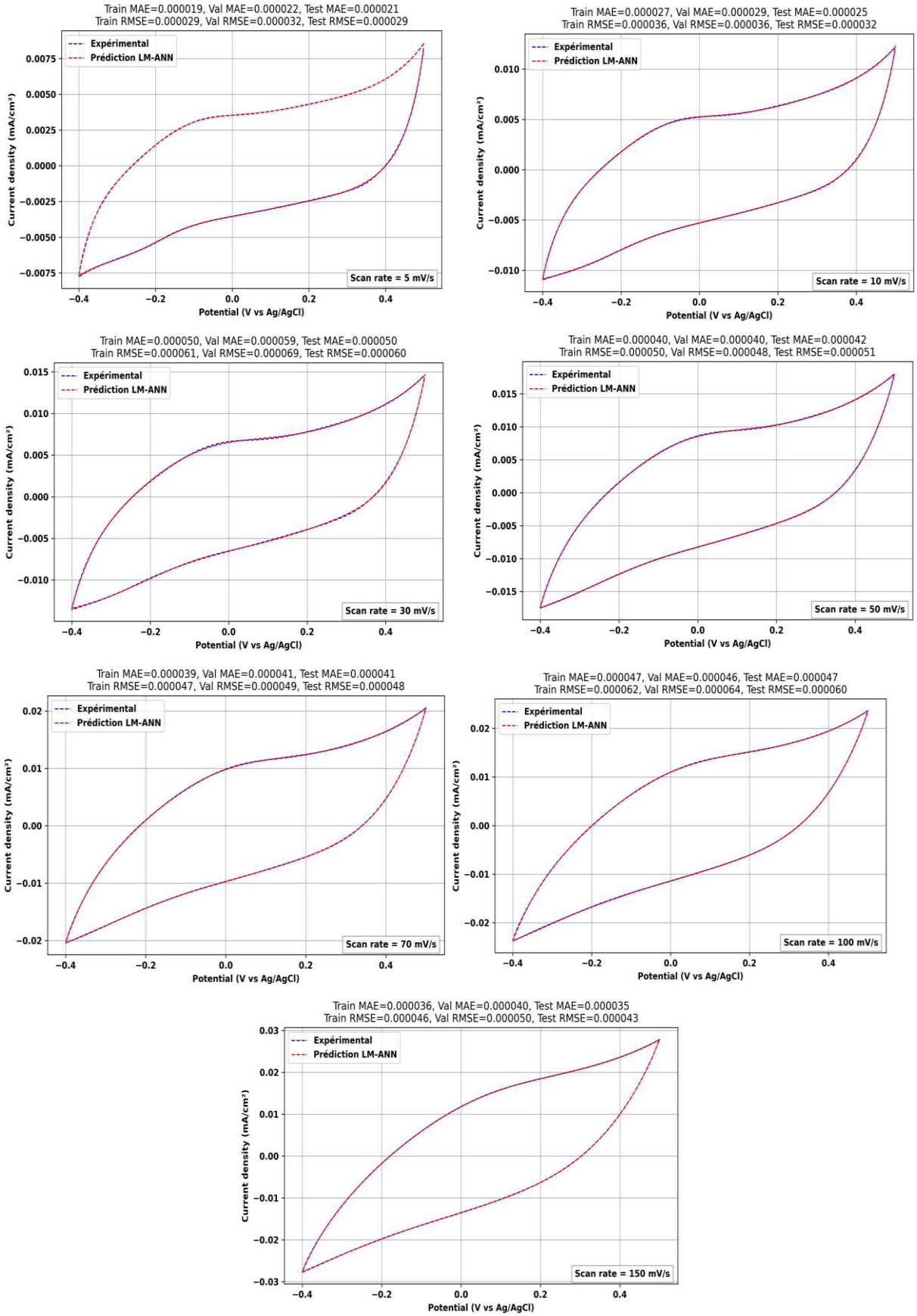


Fig. 14. Comparison between experimental and ANN predicted cyclic voltammetry curves of the $MnCo_2O_4$ supercapacitor electrode at scan rates of 5, 10, 30, 50, 70, 100 and 150 mV s^{-1}.

4. Conclusions

This study shows that NH_4F assisted synthesis effectively tailors the morphology and enhances the electrochemical performance of $MnCo_2O_4$ (MCO) nanostructures for supercapacitor applications, as confirmed by XRD, FTIR, and SEM analysis. The addition of NH_4F transforms nanowires into interconnected nanosheet arrays, increasing the electroactive surface area and facilitating efficient ion diffusion. This structural modification directly contributes to higher specific capacitance, lower charge transfer resistance and improved ionic transport, as confirmed by cyclic voltammetry (CV), electrochemical impedance spectroscopy (EIS) and galvanostatic charge-discharge (GCD) measurements. Optimized MCO-15 exhibit superior capacitance and rate capability due to their nanosheet morphology, which promotes faster ion intercalation and redox activity, while maintaining excellent long-term cycling stability. This MCO-15 electrode exhibits the highest specific capacitance by ANN with 318 Fg^{-1} for 5mV s^{-1} with a minimum error of approximately 0.01%. In addition, the proposed ANN model shows strong learning efficiency and reliable predictive performance. The close agreement between the experimental data and the ANN estimated value is confirmed by the low error percentage, the very small root mean squared error (RMSE approaching zero) and the high regression factor R^2 (around 1). These results demonstrated the robustness and accuracy of the developed ANN modes. Overall, the finding indicate that the proposed intelligent approach is well suited for predicting the cycling voltammetry behavior of supercapacitor electrodes. Looking forward, future research may focus on extending the ANN approach to predict additional electrochemical properties of MCO-15 electrode, such as electrochemical impedance and galvanostatic charge-discharge behavior. This can be achieved by modifying the input and output parameters and appropriately adjusting the network architecture, thereby emphasizing the flexibility and applicability of ANN based modeling in supercapacitor research.

Funding: This work was supported and funded by the Deanship of Scientific Research at Iman Mohammad Ibn Saud Islamic University (IMSIU) (grant number IMSIU-DDRSP2603).

Acknowledgments

The authors would like to acknowledge the support of the Deanship of Scientific Research at Iman Mohammad Ibn Saud Islamic University (IMSIU) (grant number IMSIU-DDRSP2603).

Author contributions

This work was carried out by the following co-authors from the Laboratory of Nanomaterials and Systems for Renewable Energies (LaNSER) of the Research and Technology Center of Energy (CRTEn):

- Imene Gritli, (Doctor in LaNSER of the CRTEn), played a key role in the experimental part, in the analysis and interpretation of the results and writing.

- Idoumou Bouya Ahmed (PhD student at the LaNSER laboratory of the CRTEn), played a key role in analyzing the results, particularly in analyzing the electrochemical properties.

-Dr. Zakarya Ahmed (Associate professor at IMAMU) played a key role in the Data analysis and visualization, He is also the corresponding author of this work.

- Dr. Chamsedine Maatki (Associate professor at IMAMU) and Fehri Krout played a key role in the Software modelisation and validation and carried out the computational analyses.

- Dr. Ibtissem Ben Assaker (Associate Professor at the LaNSER laboratory of the CRTEn), played a key role during the research phase, editing and approval of the final version of the manuscript.

Declarations

Competing interests

The authors declare no competing interests.

Data Availability Statement:

The datasets generated and/or analyzed during the current study are available from the corresponding author upon reasonable request.

References.

1. Liu, S., Hui, K. S. & Hui, K. N.1 D hierarchical $MnCo_2O_4$ nanowire@ MnO_2 sheet core–shell arrays on graphite paper as superior electrodes for asymmetric supercapacitors. *ChemNanoMat*. **1**, 593-602 (2015).

2. Islam, S. et al. Ahammad, Recent advancements in electrochemical deposition of metal-based electrode materials for electrochemical supercapacitors. *Chem. Rec.* **22**, e202200013 (2022).

3. Volfkovich, Y. M. Electrochemical supercapacitors. *Russ. J. Electrochem*. **57,** 311-347 (2021).

4. Bhatt, M., Gupta, B. & Sinha, A. Superior charge storage performance of optimized nickel cobalt carbonate hydroxide hydrate nanostructures for supercapacitor application. *Sci. Rep.* **15**, 2192 (2025).

5. Farid, H. M. T. et al. Facile synthesis of $CuCo_2O_4$ spinel with rGO nanocomposite via hydrothermal approach for solid state supercapacitor application. *J. Energy Storage.* **66**, 107394 (2023).

6. Norouzi, Z., Mahmoudi Najafi, S. & Mozaffari. Facile one-pot synthesis of binder-free $MnCo_2O_4$ nanosheets as efficient supercapacitor electrode material. *Prog. Color Color. Coat.* **16,** 271-281 (2023).

7. Sun, H. et al. Sonochemical synthesis of battery-type $ZnCo_2O_4$ electrode material with huge specific surface area for advanced hybrid supercapacitors. *J. Energy Storage*. **76**, 109780 (2024).

8. Jituri, S. et al. Chemically synthesized $ZnFe_2O_4$ electrodes for electrochemical oxygen evolution reaction and supercapacitor applications. *J. Mater. Sci.: Mater. Electron.* **34**, 1842 (2023).

9. Puratchimani, M., Venkatachalam, V., Rajapriya, M. & Thamizharasan, K. High Performance of $NiMn_2O_4$ Nanostructured Electrode for Supercapacitor Applications. *Anal. Bioanal. Electrochem.* **14**, 968-979 (2022).

10. Al-Rubaye, S. et al. Electrochemical performance enhancement in $MnCo_2O_4$ nanoflake/graphene nanoplatelets composite. *J. Power Sources.* **324**, 179-187 (2016).

11. Du, X. Q., Su, H. & Zhang, X. S. 3D $MnCo_2O_4$@CoS nanoarrays with different morphologies as an electrocatalyst for oxygen evolution reaction. *Int. J. Hydrog. Energy*. **44**, 21637-21650 (2019).

12. Yongzhi, M., Qingkai, B. & Kai, W. Two-step synthesis and characterization of $MnCo_2O_4$ composite and its electrochemical performance. *Int. J. Electrochem*. Sci. **13**, 10207-10216 (2018).

13. Velmurugan, M. & Chen, S.-M. Synthesis and characterization of porous $MnCo_2O_4$ for electrochemical determination of cadmium ions in water samples. *Sci. Rep*. **7**, 653 (2017).

14. Waghmode, R., Gaikwad, N., Kim, J.-R. & Maile, N. An NH_4F-assisted chemical bath synthesis of $NiCo_2O_4$ nanoforms onto stainless-steel substrate as supercapacitor electrode. *Ionics*. **30**, 4193-4202 (2024).

15. Chen, Y. et al. Wang, High-performance supercapacitor and lithium-ion battery based on 3D hierarchical NH_4F-induced nickel cobaltate nanosheet–nanowire cluster arrays as self-supported electrodes. *Nanoscale*. **5**, 9812-9820 (2013).

16. Zeng, S. et al. Sun, kinetically controlled synthesis of bismuth tungstate with different structures by a NH_4F assisted hydrothermal method and surface-dependent photocatalytic properties. *J. colloid interface sci.* **432**, 236-245 (2014).

17. Liu, T., Wang, C., Zhu, F. & Meng, Y. Morphology control and capacitive performance of Co_3O_4 nanostructures synthesized by NH_4F-assisted hydrothermal on Ni foam. *J. Mater. Sci.: Mater. Electron*. **34**, 2284 (2023).

18. Al-Rubaye, S. et al. Electrochemical performance enhancement in $MnCo_2O_4$ nanoflake/graphene nanoplatelets composite. *J. Power Sources*. **324**, 179-187 (2016).

19. Wang, B., Wang, C., Hu, Q., Zhang, L. & Wang, Z. Modeling the dynamic self-discharge effects of supercapacitors using a controlled current source based ladder equivalent circuit. *J. Energy Storage.* **30**, 101473 (2020).

20. Alimi, A. et al. Electrochemical synthesis of MnO_2/NiO/ZnO trijunction coated stainless steel substrate as a supercapacitor electrode and cyclic voltammetry behavior modeling using artificial neural network. *Int. J. Energy Res.* **46**, 17163-17179 (2022).

21. Ren, J. Engineering early prediction of supercapacitors' cycle life using neural networks. *Mater. Today, Energy*. **18**, 100537 (2020).

22. Tawfik, W.Z., Mohammad, S.N., Rahouma, K.H., Tammam, E. & Salama, G.M. An artificial neural network model for capacitance prediction of porous carbon-based supercapacitor electrodes. *J. Energy Storage*. **73**, 108830 (2023).

23. Norouzi, Z., Najafi, S. M. & Mozaffari, S. Facile one-pot synthesis of binder-free $MnCo_2O_4$ nanosheets as efficient supercapacitor electrode material. *Progress in Color, Colorants and Coatings*. **16**, 271-281 (2023).

24. Rajput S., & Rath, C. Investigation of local structure by X-ray absorption fine structure and magnetic properties of $CoMn_2O_4$ nanoparticles. *Bull. Mater.* Sci. **47**, 207 (2024).

25. Naresh, B., Kuchi, C., Rajasekhar, D. & Reddy, P. S. Solvothermal synthesis of $MnCo_2O_4$ microspheres for high-performance electrochemical supercapacitors. *Colloids Surf., A*. **640**, 128443 (2022).

26. Du, X., Su, H. & Zhang, X. 3D $MnCo_2O_4$@ CoS nanoarrays with different morphologies as an electrocatalyst for oxygen evolution reaction. *Int. J. Hydrogen Energy*. **44**, 21637-21650 (2019).

27. Yongzhi, M., Qingkai & Kai, B.W. Two-step synthesis and characterization of $MnCo_2O_4$ composite and its electrochemical performance. *Int. J. Electrochem. Sci*. **13**, 10207-10216 (2018).

28. Waghmode, R., Gaikwad, N., Kim, J.-R. & Maile, N. An NH_4F-assisted chemical bath synthesis of $NiCo_2O_4$ nanoforms onto stainless-steel substrate as supercapacitor electrode. *Ionics.* **30***,* 1-10 (2024).

29. Antunović, V., Ilić, M., Baošić, R., Jelić, D. & Lolić, A. Synthesis of $MnCo_2O_4$ nanoparticles as modifiers for simultaneous determination of Pb (II) and Cd (II). *PloS one*. **14**, e0210904 (2019).

30. Cheng, L., Xu, M., Zhang, Q., Li, G., Chen, J. & Lou, Y. NH_4F assisted and morphology-controlled fabrication of $ZnCo_2O_4$ nanostructures on Ni-foam for enhanced energy storage devices. *J. Alloys Compd.* **781**, 245-254 (2019).

31. Liu, D., Liu, Y., Liu, X., Xu, C., Zhu, J. & Chen, H. Growth of uniform $CuCo_2O_4$ porous nanosheets and nanowires for high-performance hybrid supercapacitors. *J. Energy Storage*. **52**, 105048 (2022).

32. Radhi, A.A., Al-rubaiey, S.I.J. & Al-Rubaye, S. NH_4F-assisted and morphology-controlled fabrication of iron cobaltite $FeCo_2O_4$ nanoparticles on carbon fiber cloth for supercapacitor applications. **78**, *Chem. Pap.* 733-746 (2024).
33. Lamouchi, A., Assaker, I. B. & R. Chtourou, Enhanced photoelectrochemical activity of MoS_2-decorated ZnO nanowires electrodeposited onto stainless steel mesh for hydrogen production. *Appl. Surf. Sci***. 478**, 937-945 (2019).
34. Husain, A. et al. Attaining promising efficiency through a Quasi-Solid-State symmetrical supercapacitor and dye-sensitized solar cell counter electrode utilizing bifunctional Nitrogen-Doped microporous activated carbon. *Inorg. Chem. Commun.* **168**, 112859 (2024).
35. Ahmed, I. B. et al. Supercapacitive performance of 3D-cobalt oxide (Co_3O_4) nanowires grown onto anodized stainless-steel substrate: effect of anodization time. Solid State Sci. **152**, 107537 (2024).
36. Shahmohammadi, A., Dalvand, S. & Baheri, H. Electrochemical synthesis of hybrid nanostructure of nickel cobalt phosphide/molybdenum disulfide on nickel foam as an effective electrode material in supercapacitor. **317**, *Mater. Chem. Phys***.** 129150 (2024).
37. Zhang, W. et al. Construction of superior performance $LiVPO_4F$/C cathode assisting by a regulating additive NH_4F and the "Combination-Protection-Release" mechanism for lithium-ion batteries. *J. Power Sources*. **523**, 231024 (2022).
38. Aouini, S. et al. Synthesis and characterization of $CoMn_2O_4$ spinel onto flexible stainless-steel mesh for super-capacitor application. *Solid State Sci.* **143**, 107283 (2023).
39. Ramachandran, T. et al. KOH mediated hydrothermally synthesized hexagonal-$CoMn_2O_4$ for energy storage supercapacitor applications. *Int. J. Energy Res.**46**,* 16823-16838 (2022).
40. Sowmiya, K. & Vijayalakshmi, K. Refining the Integration Strategy for $CoMn_2O_4$ Nanostructures to Maximize Their Effectiveness in Supercapacitor Functionalities. *J. Electron. Mater*. **54**, 1-9 (2024).
41. El Nady, J. et al. One-step electrodeposition of a polypyrrole/NiO nanocomposite as a supercapacitor electrode. *Sci. Rep.* **12**, 3611 (2022).
42. Xiong, Y. Carbon cathode with heteroatom doping and ultrahigh surface area enabling enhanced capacitive behavior for potassium-ion hybrid capacitors. *Rare Met*. **43**, 2136-2149 (2024).
43. Zhang, Z. et al. Carbon-coated $Li_4Ti_5O_{12}$ optimized by fluorine regulation strategy for high-rate lithium-ion batteries with mixed diffusion and capacitive effects. *Carbon*. **221**, 118885 (2024).
44. Jia, D. et al. In situ electrochemical tuning of MIL-88B (V)@ rGO into amorphous V_2O_5@ rGO as cathode for high-performance aqueous zinc-ion battery. Advanced Functional Materials. **34**, 2308319 (2024).
45. Nallapureddy, J. et al. Morphology controlled synthesis of $MnCo_2S_4$ nanoflower structures for different metal precursors used for energy storage applications. *J. Power Sources*. **613**, 234883 (2024).
46. Tan, Z. et al. Efficient capacitive deionization with hierarchical porous carbon flow electrodes. *Desalination*, **591**, 118051 (2024).
47. R. Hasan, et al. ZnS@ Fe_2O_3 core–shell nanorod arrays for supercapattery applications; theoretical evaluation of faradic and non-faradic behavior using Dunn's model. *J. Electroanal. Chem*. **966**, 118411 (2024).
48. Li, R. et al. N-Doped Carbon Coated Bimetallic $CoFe_2O_4$ Nanomembranes as An Enhanced Negative Electrode for Asymmetric Supercapacitors. *ChemNanoMat*. **10**, e202400176 (2024).

49. Yao, S. et al. In situ grown hierarchical NiO nanosheet@ nanowire arrays for high-performance electrochromic energy storage applications. *Nanoscale Adv.* **4**, 4748-4755 (2022).
50. Xu, J. et al. Fabrication of the porous $MnCo_2O_4$ nanorod arrays on Ni foam as an advanced electrode for asymmetric supercapacitors. *Acta Mater*. **152**, 162-174 (2018).
51. Che, H., Liu, A., Mu, J., Wu, C. & X. Zhang. Template-free synthesis of novel flower-like $MnCo_2O_4$ hollow microspheres for application in supercapacitors. *Ceram. Int.* **42**, 2416-2424 (2016).
52. Gopi, C. V., Venkata-Haritha, M., Kim, S.-K., Prabakar, K. & H.-J. Kim. Flower-like ZnO@$MnCo_2O_4$ nanosheet structures on nickel foam as novel electrode material for high-performance supercapacitors. *RSC Adv.***6**, 102961-102967 (2016).
53. Anjana, P., Kumar, S. S. & R. Rakhi, $MnCo_2O_4$ nanoneedles self-organized microstructures for supercapacitors. *Mater. Today Commun.* **28**, 102720 (2021).
54. Kuang, L. et al. Mesoporous $MnCo_2O_{4.5}$ nanoneedle arrays electrode for high-performance asymmetric supercapacitor application. *Biochem. Eng. J*. **315**, 491-499 (2017).
55. Maile, N. C. et al. Structural and morphological changes in binder-free $MnCo_2O_4$ electrodes for supercapacitor applications: effect of deposition parameters. *J. Mater. Sci.: Mater. Electron*. **30**, (2019) 3729-3743.
56. Zhu, Z. et al. In-situ growth of $MnCo_2O_4$ hollow spheres on nickel foam as pseudocapacitive electrodes for supercapacitors. *J. Colloid Sci.* **587**, 56-63 (2020).
57. Tawfik, W.Z., Mohammad, S.N., Rahouma, K.H., Tammam, E. & Salama, G.M., An artificial neural network model for capacitance prediction of porous carbon-based supercapacitor electrodes, *J. Energy Storage.* **73**, 108830 (2023)
58. Adekoya, G.J. et al. A mini-review of artificial intelligence techniques for predicting the performance of supercapacitors. Mater. *Today Proc.* **62**, S184-S188 (2022).